Annual Review of Nuclear and Particle Science

Novel Liquid Argon Time-Projection Chamber Readouts

Jonathan Asaadi,[1] Daniel A. Dwyer,[2] and Brooke Russell[2,3]

[1]Department of Physics, University of Texas at Arlington, Arlington, Texas, USA; email: jonathan.asaadi@uta.edu

[2]Physics Division, Lawrence Berkeley National Laboratory, Berkeley, California, USA; email: dadwyer@lbl.gov

[3]Laboratory for Nuclear Science, Massachusetts Institute of Technology, Cambridge, Massachusetts, USA; email: russell3@mit.edu

Annu. Rev. Nucl. Part. Sci. 2024. 74:529–55

First published as a Review in Advance on July 10, 2024

The *Annual Review of Nuclear and Particle Science* is online at nucl.annualreviews.org

https://doi.org/10.1146/annurev-nucl-102422-035255

Keywords

time-projection chambers, liquid argon, cryogenic detectors, particle detectors, readout electronics

Abstract

Liquid argon time-projection chambers (LArTPCs) have become a prominent tool for experiments in particle physics. Recent years have yielded significant advances in the techniques used to capture the signals generated by these cryogenic detectors. This article summarizes these novel developments for detection of ionization electrons and scintillation photons in LArTPCs. New methods to capture ionization signals address the challenges of scaling traditional techniques to the large scales necessary for future experiments. Pixelated readouts improve signal fidelity and expand the applicability of LArTPCs to higher-rate environments. Methods that leverage amplification in argon enable measurements in the keV regime and below. Techniques to enhance collection of argon scintillation photons improve calorimetry and expand the physics program for very large detectors. Future efforts aim to demonstrate systems for the combined detection of both electrons and photons.

Contents

1. INTRODUCTION

Liquid argon time-projection chambers (LArTPCs) combine high-resolution tracking and calorimetry in a dense, fully active detector. For this reason they have found a wide range of applications in nuclear and particle physics. This increase in use has driven commensurate advances in the techniques used to sense and record the signals produced in these detectors. In this article, we review these novel developments for LArTPC readout.

In Section 2, we review the basic characteristics of LArTPCs and provide a brief summary of the characteristics of liquid argon ionization and scintillation. The historical context for LArTPC development is outlined in Section 3. Section 4 presents developments in the detection of free electrons from ionization. Progress in scintillation light detection is discussed in Section 5. Section 6 summarizes novel efforts toward integrated systems that are sensitive to both electrons and photons. Concluding remarks are given in Section 7.

2. LIQUID ARGON TIME-PROJECTION CHAMBER BASICS

At its core, a LArTPC consists of a uniform volume of argon held in the liquid state. In response to ionizing radiation, argon generates scintillation photons as well as free electrons. Detection of the scintillation photons typically allows one to determine, with a precision of $\mathcal{O}(1)$ ns, the time at which the detector was ionized; it can also provide calorimetric information for detectors with sufficient photocoverage and efficiency. An electric field is applied across the argon volume, drifting the free electrons to an anode at velocities of $\mathcal{O}(1)$ mm μs^{-1}. The anode is instrumented to be sensitive to the spatial distribution of electrons across the anode surface, typically with a granularity of $\mathcal{O}(1)$ mm. This 2D spatial distribution combined with its 1D time of arrival at the anode provides a 3D image of the distribution of free electrons—hence the name time-projection chamber (TPC). Consequently, LArTPCs can provide both high-fidelity calorimetry and 3D tracking within a fully active detector volume. The ratio of ionization electron to scintillation photon production varies with particle ionization density and electric field strength; this property of noble liquids has been

crucial for particle discrimination and background rejection for rare event searches (1). This combination of characteristics makes LArTPCs a preferred detector for a wide range of applications, as summarized in the experimental methods section of Reference 2.

For the design of LArTPC readout systems, it is important to understand the detailed characteristics of the signals. Approximately 4.2×10^4 free electrons are produced per MeV of energy deposited in liquid argon (W value = 23.6 eV per electron) (3). A significant fraction of these electrons are immediately lost due to recombination with ions. Losses increase with ionization density and decrease with drift field strength (4, 5). For minimum ionizing particles (MIPs) in liquid argon ($\mathrm{d}E/\mathrm{d}x = 2.12$ MeV cm^{-1}) and typical drift field strengths of 500 V cm^{-1}, the recombination loss is roughly 30%. The most probable MIP energy loss is slightly lower [$(\mathrm{d}E/\mathrm{d}x)_{\mathrm{MPV}} = 1.63$ MeV cm^{-1}], resulting in a most probable ionization signal yield of roughly 5×10^3 electrons per millimeter of MIP track length after recombination. Trace amounts (ppb to ppt) of electronegative impurities (e.g., O_2, H_2O) in the argon can capture electrons during their drift to the anode, resulting in further losses if not managed (6).

Scintillation photon yields are similar at 5×10^3 photons per millimeter of MIP track length, given the W value of 19.5 eV per photon (7) and recombination losses of 56% (8) at MIP energy densities and a drift field of 500 V cm^{-1}. Scintillation photon emission is isotropic and peaks at ∼127 nm (9, 10). It is composed of a fast component [$\mathcal{O}(1)$ ns] and a slow component[1] [$\mathcal{O}(1)$ μs]; the relative proportion varies with ionization density and electric field strength (11). Liquid argon is effectively transparent to its scintillation, but the Rayleigh scattering length[2] is $\mathcal{O}(1)$ m (12).

The TPC itself is immersed in liquid argon surrounding the region of interest. The TPC typically consists of a cathode and anode in an arrangement similar to a parallel-plate capacitor (**Figure 1**). A potential difference between them generates the electric field that drifts the free electrons to the anode. Electron drift velocity in liquid argon is 1.6 mm μs^{-1} at a field strength of 500 V cm^{-1} and 87 K; it increases with field strength and decreases with temperature (13). In transit, the electrons diffuse both transversely and longitudinally to the drift direction, typically $\mathcal{O}(1)$ mm per meter of drift (14, 15). Field-shaping panels surround the gaps between anode and cathode edges to improve drift field uniformity. Field uniformity is important for minimizing spatial distortions during electron drift as well as biases to drift velocity and recombination. At standard atmospheric pressure, argon is liquid ($\rho = 1.4$ g cm^{-3}) in a narrow range of temperatures, between 83.8 and 87.3 K (16). For this reason, a LArTPC is generally operated within a cryostat with the capabilities to maintain the system pressure and temperature within this regime.

Existing LArTPCs typically fall into one of two broad classes based on their scientific needs. The first class prioritizes accurate spatial imaging of high-energy (≫MeV) particle interactions and has been successfully used to measure the rare interactions of neutrinos with nuclei. The second class prioritizes optimal calorimetry at keV to MeV energies, enabling searches for phenomena such as dark matter coherent nuclear scattering and neutrinoless double-beta decay. This review focuses primarily on recent developments for detectors in the former class, but these efforts may also find use in the latter class.

3. HISTORICAL CONTEXT

Throughout the 1960s, bubble and spark chambers were the technology of choice for tracking detectors in high-energy physics (17). In the late 1960s, two groundbreaking innovations emerged almost simultaneously: the multiwire proportional chamber (18) and the drift chamber (19). Along with the rapid advancement in semiconductor electronics, which had begun merely a decade

[1] Specific values of the scintillation decay times show significant variation in the literature.
[2] Reported measurements and calculations vary from roughly 0.5 to 1 m.

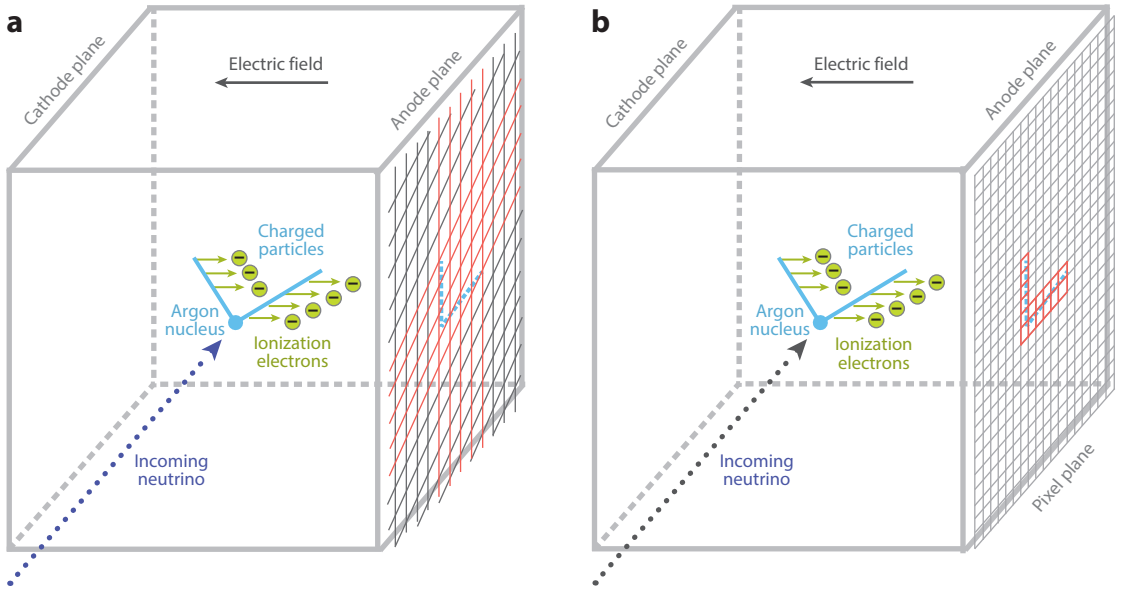

Figure 1

Conceptual diagrams of two LArTPCs. In both cases, a neutral particle (*dotted arrow*) interacts with an argon nucleus (*blue circle*), generating charged particle tracks (*blue lines*) that free ionization electrons (*green circles*). Applying a potential difference between the cathode and anode produces an electric field that drifts the free electrons to a sensitive anode instrumented with (*a*) two planes of wire arrays or (*b*) a pixelated readout system. Abbreviation: LArTPC, liquid argon time-projection chamber. Figure provided by R. Soleti.

earlier, these technologies paved the way for the speedy readout of hundreds, and soon thousands, of signal channels at an economically feasible cost. This breakthrough was a crucial factor that fueled the remarkably swift evolution of these detector technologies. Many diverse designs were explored, and the designs continuously increased in size and complexity. In 1974, Dr. David Nygren, a physicist at Lawrence Berkeley National Laboratory, introduced the TPC, a type of drift chamber that offered simultaneous nonprojective track recognition, momentum measurement, and particle identification within a compact apparatus (20). This innovation aimed to address the challenges of precisely detecting and characterizing charged particles in high-energy physics experiments. The first experiment in particle physics to use a TPC was designed in 1976 at SLAC for the PEP-4 collider. Its success led to a long list of subsequent collider-based experiments using the technology as outlined in Reference 21 and the references cited within. Further exploitation of the favorable properties was shown by William J. Willis and Veljko Radeka in the deployment of an ionization chamber for total-absorption calorimeters (22), which has been further exploited in numerous subsequent detectors over the decades (23).

In 1977, physicist Carlo Rubbia proposed using ultrapure liquid argon as the medium for the TPC (24). This proposal drew on the notion that in high-purity noble liquids, ionization electrons can be drifted over large distances and imaged by position-segmented electrodes at the end of the drift path. This led to the first large-scale liquid argon neutrino experiment, which was named ICARUS (Imaging Cosmic and Rare Underground Signals). The detector was initially commissioned during a surface run in a laboratory in Pavia, Italy, in 2001 (25), and the full 760-ton LArTPC was deployed in Gran Sasso Laboratory between 2010 and 2013 and exposed to the CNGS (CERN Neutrinos to Gran Sasso) beam (26). In the intervening time between its first proposal and the first experimental run, TPCs based on liquefied noble elements were used in

a large number of particle physics experiments—especially for rare event detection, such as dark matter (27) and neutrinoless double-beta decay (28) searches.

Concurrently with these efforts, a large-scale US-led research program into the use and advancement of LArTPCs began. The first US LArTPC to collect neutrino data was the ArgoNeuT (Argon Neutrino Teststand) experiment (29). This was a small, 0.77-ton LArTPC that ran in the NuMI (Neutrinos from the Main Injector) beamline from 2009 to 2010. This was followed by the Micro Booster Neutrino Experiment (MicroBooNE) (30)—a 170-ton LArTPC with a primary aim of investigating the anomaly of electromagnetic shower signatures seen by the MiniBooNE experiment (31). The experimental success of ArgoNeuT and MicroBooNE paved the way for a physics program using LArTPCs for short-baseline and long-baseline neutrino oscillation studies (32, 33) and launched a robust set of R&D activities (34–38) to improve on the detector concepts and designs pioneered over the last 40 years. Concurrent with this has been extensive R&D into cryogenic-compatible dedicated charge readout electronics deployed in the detector. These advancements have pushed the detection threshold and signal-to-noise ratios of these detectors to ever-increasing sensitivities. This work is well summarized in Reference 39. While the above advances have focused on the development of argon-based TPCs and their application to neutrino experiments, similar rapid advances have been made in their application as a tool to search for dark matter and other faint signals by the WArP (40), MiniClean (41), DEAP (42), and DarkSide (43) collaborations. The following sections highlight some of the recent developments, broadly classified into advancements made in the detection of ionization signals and in the detection of scintillation photons. It is worth noting that, although absent from this review due to length restrictions, significant progress has also been made in the engineering and operations of these detectors, which has allowed them to scale up in size and sensitivity. From the cryogenic infrastructure, purification techniques, and long-term operations, the amount of progress and understanding to make the TPC a key technology in high-energy physics has been quite impressive.

4. DEVELOPMENTS IN IONIZATION ELECTRON DETECTION

LArTPCs are instrumented to detect and record the quantity, 2D position, and time of arrival of ionization electrons at the anode, typically with millimeter and microsecond granularity, respectively. The most common readout technique for single-phase LArTPCs involves arrays of evenly spaced wires coplanar with the anode. (Dual-phase LArTPCs, where ionization electrons are extracted from the liquid-to-gas phase for measurement, are discussed in Section 4.3.2.) The drift of electrons into the vicinity of a wire induces a current according to the Shockley–Ramo theorem (44, 45), and this signal is typically amplified and recorded using custom electronics. A single array of wires records a 2D distribution of ionization electrons, where one spatial coordinate is given by the position of each wire in the array, and the other coordinate is given by the electron drift time. The anode is instrumented with a sandwich of multiple arrays, typically three, and each array's wires are oriented at a different angle in the plane of the anode. To ensure that signals are induced on each array, an electrical bias is applied between each layer to avoid collection of the drifting electrons on all but the final layer, a condition referred to as electron transparency. This typically results in induced signals that are unipolar on the final array and bipolar on the others. The 2D distributions from each array are combined to estimate the underlying 3D distribution of electrons. Multiple signals arriving simultaneously at different locations on the anode introduce ambiguities in this estimation and can be very challenging to overcome for complex ionization distributions such as particle showers. Another issue is that tracks oriented near-normally to the anode effectively vanish from the noncollection layers. This can be understood as follows: The signal induced by electrons approaching a given wire in the noncollection array is canceled by the opposite-polarity signal of electrons drifting away from that wire. So, for a minimum ionizing

track that is near-normal to the anode, only changes in the ionization density (primarily the start and end of the track) are evident on a given wire on the noncollection layers, while the full signal is registered on the collection layer. There has been significant recent progress in signal-processing techniques to address these issues, including signal noise filtering (30) and deconvolution (46, 47).

4.1. Strip-Based Anodes

Strip-based anodes, where wire arrays are replaced with arrays of conductive strips etched on fiberglass sheets (**Figure 2**), have been a focus of recent development. While strip-based detectors have a long history in other applications, an important recent development has been electron-transparent strip detectors for use in LArTPCs. By perforating the strip panel at a level of ~60% and applying a strong electrical bias (e.g., 500 V) between successive layers, transparency has been demonstrated in recent prototypes (48, 49). This enables the use of multiple layers of strips to generate different 2D views in the same manner as that of wire-array anodes. The prototype assembly shown in **Figure 2*a*** consists of two fiberglass panels that are clad in a thin layer of

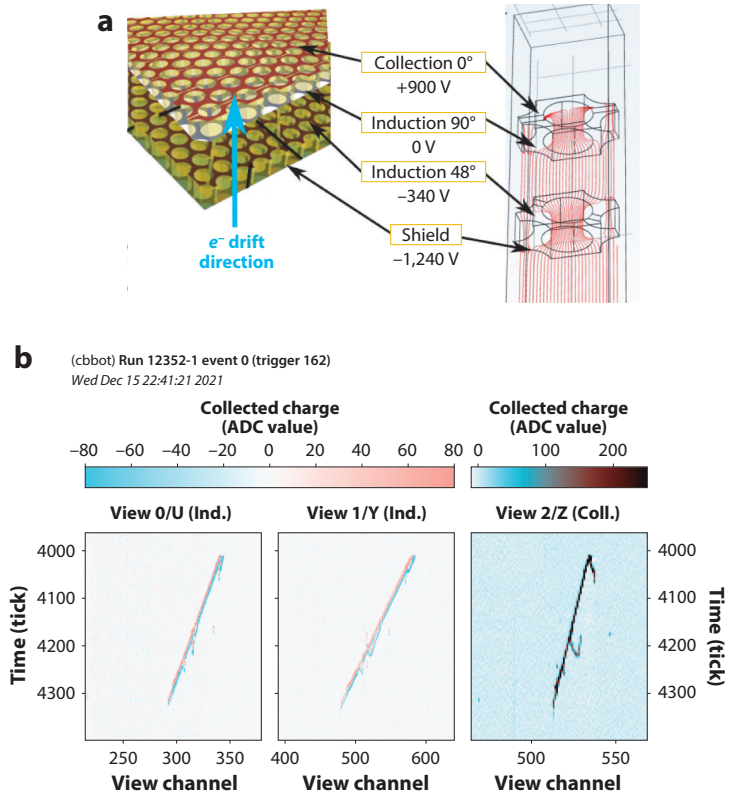

Figure 2

(*a*) Diagram of a four-layer strip-based LArTPC readout assembly, including a simulation of electron transparency. The assembly consists of two perforated fiberglass panels (*yellow*) with thin conductive copper (*red*) laminated on each face. Each copper layer has narrow etchings to produce conductive strips in different orientations on each face, visible as very thin yellow lines in the copper. Electrons drift through holes in the induction printed circuit board toward the collection plane. Panel adapted with permission from Reference 48 (CC BY-NC-ND 4.0). (*b*) A segment of a cosmic ray imaged by the three instrumented layers of the prototype. Panel adapted with permission from Reference 49 (CC BY-NC-ND 4.0). Abbreviations: ADC, analog-to-digital converter; LArTPC, liquid argon time-projection chamber.

copper on each face, similar in construction to a printed circuit board (PCB). The copper layer has narrow etchings to produce conductive strips in different orientations on each face, and each panel is perforated in a manner to ensure that these conductive strips are not interrupted. Electronics to record signals are coupled to the strips along one edge of the panel. To create strip panels that are larger than typical PCBs (>0.5 m), techniques to electrically bridge strips across the edges of adjacent panels have been developed.

Strip detectors facilitate mass production, leveraging the same techniques used to produce PCBs. They are also more mechanically robust, simplifying handling and installation, and are immune to catastrophic failure due to a broken wire electrically short-circuiting the anode. Strips have a larger capacitance per unit length relative to a wire array of similar spacing, resulting in higher noise unless this is compensated for with increased power to the associated front-end electronics or increased channel density. Overall, strip-based LArTPC anodes are viewed as a significant improvement relative to traditional wire arrays.

4.2. Pixelated Anodes

While strip-based anodes address challenges associated with scalability for very large LArTPC anodes, they are still susceptible to signal ambiguities inherent to 2D projective readout methods. To overcome these signal ambiguities, there has been recent progress in the development of pixelated anodes. A pixelated anode is composed of a single 2D array of conductive pixels or pads on a fiberglass panel. Instrumenting each pixel with a uniquely addressable readout provides direct sensitivity to the distribution of electrons in the plane of the anode. Including sensitivity to the drift time, this readout provides native 3D imaging of the distribution of ionization in the LArTPC.

While pixel- or pad-based anodes have long been used in gaseous TPCs, the channel densities required for LArTPCs [e.g., $\mathcal{O}(10^5)$ channels per square meter at 3-mm granularity] present technical challenges regarding signal multiplexing and waste heat. Efforts to address these challenges are discussed below. As a benefit, pixels have significantly lower capacitance, typically a few picofarads, relative to wires and strips. This allows for less power consumption in the front-end amplifier to achieve an equivalent level of noise, which can compensate for the far greater channel density. It also reduces the depth of view into the LArTPC for signal induction on the pixel relative to wires or strips. A pixelated anode also requires no transparency and therefore benefits from simpler unipolar signals. Consequently, signal deconvolution is far simpler for pixelated LArTPCs. The first demonstration of a LArTPC with a pixelated anode occurred only recently (50). Given the lack of suitable low-power electronics, it required merging of the signals from 28 pixels into each electronics channel and leveraged detection of regional induction to disambiguate pixel signals. Nonetheless, it was a positive step forward in the development of pixelated LArTPCs.

Two efforts on pixelated readout are presented in this section: LArPix and Q-Pix. The LArPix system is designed for true 3D imaging of the distribution of ionization electrons. It has been used to instrument multiple ton-scale prototype detectors with $\mathcal{O}(10^5)$ pixels, demonstrating the viability of large-scale pixelated readout for LArTPCs. Q-Pix is a novel concept in development with the potential to record both electrons and photons. The Q-Pix concept and its application for electron detection are discussed in this section, while the development of this concept for photon detection is presented in Section 6.

4.2.1. LArPix. LArPix is an end-to-end charge readout system for large-scale, $\mathcal{O}(10^7)$-channel, millimeter-granularity LArTPC anode pixelization. The system architecture is composed of tileable 6,400-channel large-format anode PCBs, cryogenic-compatible data and power cabling, cryostat feedthrough assemblies, and multitile digital controllers. All components within the

Table 1 LArPix-v2 system specification summary

Specification	Value	Comment
ASIC		
Analog inputs	64	Single-ended
Gain	4 μV per electron (nominal)	Optional 2 μV per electron mode
Noise	<800 e^- ENC	—
Power	2×10^{-4} W per channel	—
Dynamic range	1.2	3×10^5 e^- at nominal gain
ADC resolution	8 bits	—
ADC LSB	4 mV (nominal)	—
Threshold range	0–1.8 mV	—
Time-stamp precision	100 ns	At 10-MHz nominal clock
Operating temperature	80–300 K	—
Anode tile		
Dimensions	31 × 32 cm	—
Number of pixels	6,400	—
Pixel pitch	3.8 mm	—
Noise injection	<100 e^- ENC	—
Controller		
Power	42 W	Driving 8 anode tiles
I/O channels	32	—
Digital power stability	<1%	—
Analog power stability	<1%	—
Noise injection	<250 e^- ENC	—
Pixel multiplexing	1,600 per I/O (nominal)	16,320 per I/O (maximum)

Abbreviations: ADC, analog-to-digital converter; ASIC, application-specific integrated circuit; ENC, equivalent noise charge; LSB, least significant bit.

LArPix system are compatible with large-scale commercial production techniques, enabling low-cost, quick-turn component production at $\mathcal{O}$($0.10) per channel (approximately $10,000 per square meter). Performance, manufacturability, and reliability drive system design. The three principal components of the system—the LArPix application-specific integrated circuit (ASIC), the large-format anode tile, and the warm electronics controller—are described here. **Table 1** summarizes the specifications for each component. LArPix has been developed as the baseline technology of the Deep Underground Neutrino Experiment (DUNE) Liquid Argon Near Detector (ND-LAr) (51).

The key element of the system is the ASIC, a mixed-signal detector system-on-a-chip implemented in 180-nm CMOS technology. The LArPix-v1 ASIC (52) was a proof-of-principle demonstration of a highly multiplexed, low-power, cryo-compatible pixelated charge readout technology on the 1,000-channel scale. Each of the 32 channels on the LArPix-v1 ASIC operated as an independent self-triggering signal processor. The LArPix-v1 ASIC demonstrated a custom low-power amplifier and channel self-triggering, averaging 62 μW per channel, mitigating risks associated with waste heat inadvertently boiling the argon in the detector. Multiple 33-mm^2 LArPix-v1 bare die were mounted directly on an anode PCB for an $\mathcal{O}$(1,000)-channel LArTPC, and this system was successfully used to image cosmic rays. However, the readout was difficult to mass produce, underscoring the need for system scalability and robustness.

The LArPix-v2 system was designed to ease large-scale production and operation. Each v2 ASIC has 64 analog input channels, and each of these includes an integrating charge-sensitive amplifier (CSA), a tunable discriminator, and an 8-bit successive approximation register (SAR) analog-to-digital converter (ADC). A digital core for configuration and data I/O is shared across all channels. The ASIC front end is optimized for detectors with a capacitance of $\mathcal{O}(1)$ pF. Each input is coupled to a millimeter-scale conductive pixel pad on a large-format anode tile. Charge collected by the pixel is integrated and amplified by the ASIC front end with a default gain of 4 μV per electron. If the integrated charge exceeds the threshold of the tunable discriminator (which is typically set in the range of 4×10^3 to 7×10^3 e^-), the signal is captured and an analog–digital conversion is initiated. In parallel, the channel front end is reset over the period of one 10-MHz clock cycle, introducing a negligible deadtime, and is prepared to receive subsequent signals. The ASIC digital core assembles an event record of each trigger noting the ADC value (8-bit resolution), threshold-crossing time stamp (100-ns resolution at 10-MHz system clock), and channel and chip unique integer identifiers. The design provides a continuous readout of all signals above the single-pixel threshold, typically $\mathcal{O}(100)$ keV, while maintaining modest data rates. A data rate of ∼40 bytes per second per pixel has been measured in a LArTPC with 30-cm drift exposed to the cosmic-ray flux present on the Earth's surface.

Each LArPix-v2 ASIC is packaged in a 128-pin, low-profile quad flat package to facilitate pixel tile assembly through standard pick-and-place and solder reflow techniques. A novel programmable chip-to-chip I/O routing technique, called Hydra I/O, is used to enhance system reliability. Each chip can communicate with any of four neighbors, dynamically routing data around faulty chips and avoiding single-point failures.

The current prototype 31-cm by 32-cm pixel anode tile has 6,400 charge-sensitive pixels at 3.8-mm pitch on one face and 100 LArPix-v2 ASICs on the opposite face. It can be configured and read out via a single pair of custom low-voltage differential digital input and output channels, although four independent channels are provided to ensure system reliability. Pixel tiles are designed according to standard multilayer PCB layout methods, facilitating large-scale production. Careful isolation of digital and power zones within the 3-mm-thick tile prevents noise transmission into the pixels below the limit of detection (<100 e^- equivalent noise charge). Clock, trigger, and synchronization signals are fanned out to every ASIC on the anode tile. A prototype LArPix anode tile is pictured in **Figure 3*a***. To date, approximately 80 large-format anode tiles have been

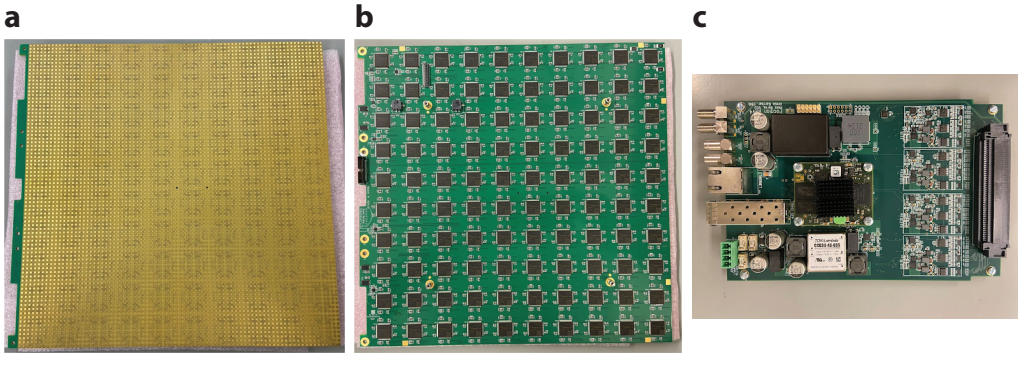

Figure 3

Prototype LArPix-v2 anode tile 31 cm in length by 32 cm in height with (*a*) 6,400 gold-plated, charge-sensitive pixel pads at 3.8-mm pitch driven by (*b*) 100 LArPix-v2 application-specific integrated circuits. (*c*) The Pixel Array Controller and Network (PACMAN) readout control electronics card can drive eight anode tiles.

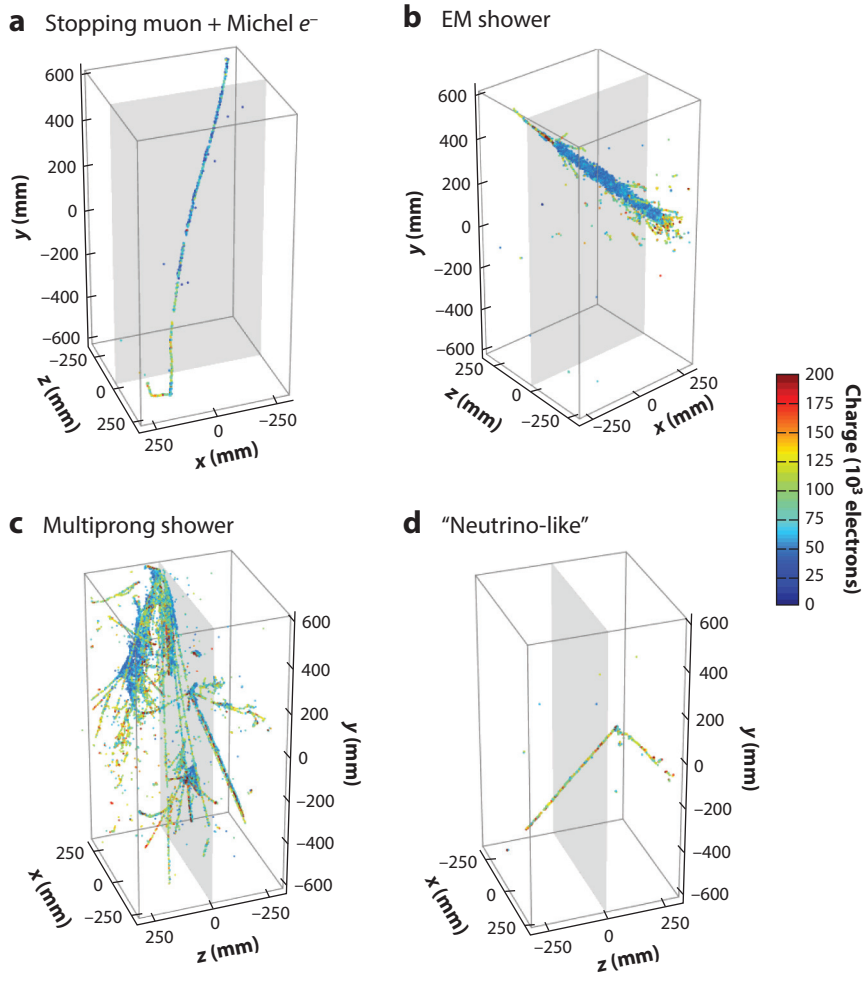

Figure 4

Cosmic-ray interactions imaged with the first of four modules of the LArPix-based 2×2 Demonstrator modular LArTPC. This first module (also called Module 0) was instrumented with 78,400 pixels at 4.4-mm pitch. Each point represents the raw data from one self-triggering and digitization cycle of a pixel; color indicates signal amplitude above baseline in approximate number of electrons. Abbreviations: EM, electromagnetic; LArTPC, liquid argon time-projection chamber. Figure adapted from Reference 53 (CC BY 4.0).

manufactured commercially, leveraging vendor-based postassembly quality control inspection. Sixty-four of these tiles have been used to instrument the 2×2 Demonstrator, a prototype of the modular LArTPC design planned for the DUNE Near Detector (51). Examples of some of the $\mathcal{O}(10^7)$ cosmic-ray images collected during the preparation of this LArTPC are shown in **Figure 4**.

The Pixel Array Controller and Network (PACMAN) readout control electronics card (**Figure 3*c***) provides power, data I/O, 10-MHz system clock, synchronization, and external triggers to eight pixel anode tiles (51,200 pixels). It includes a CPU with an integrated operating system and programmable logic. A standard TCP/IP-based ethernet connection carries configuration commands to and detector data back from the controller. PACMAN communicates

with the pixel tiles using 5-MHz serial data via low-voltage differential transmitters and receivers. The controller is mounted on the room-temperature side of a custom LArTPC cryostat feedthrough. Filtered analog and digital power is provided with 1% stability. Ground isolation is incorporated to maintain <1 mV of noise injection into the cryostat.

Future LArPix development is focused on optimizing ASIC analog performance, improving quality assurance, and extending its application to larger systems. The next ASIC version aims to reduce front-end noise and improve ADC dynamic range and resolution. ASIC resilience to repeated cryo-cycling, mitigation of cryo-aging, and resilience to environmental static discharge are currently under study.

4.2.2. Q-Pix (electrons). The fundamental idea of the Q-Pix pixel-based charge readout scheme is to use pixel-scale self-triggering charge integrate/reset (CIR) blocks with local clocks running with unconstrained frequencies and dynamically established data networks for robust resilience against single-point failure (54). The basic concepts of the Q-Pix circuit are shown in **Figure 5*a***. The input pixel is envisioned as a simple circular trace connected to the Q-Pix circuit by a PCB. The circuit begins with the CIR circuit. This CSA continuously integrates incoming signals on a feedback capacitor until a threshold on a Schmitt trigger (regenerative comparator) is met. When this threshold is met, the Schmitt trigger starts a rapid reset enabled by a MOSFET switch, which drains the feedback capacitor and returns the circuit to a stable baseline, and the cycle is free to begin again.

To mitigate any potential charge loss that can occur during a reset and to allow for the CIR circuit to keep up with arbitrarily large charge deposits, an alternative design known as the replenishment scheme has also been evaluated. In contrast to the reset architecture, in this scheme the MOSFET functions as a controlled current source such that when the Schmitt trigger undergoes a transition, the MOSFET replenishes a charge of $\Delta Q = I \cdot \Delta t$, where Δt is the reset pulse width or discharge time. This ΔQ then forms a charge quantum of each transition. Even if there is a significant input charge during the discharging process, as long as the MOSFET current and the discharge time are fixed, the quantization ΔQ of each measurement will remain constant. This allows the circuit to discharge the C_f through the MOSFET and integrate the input current simultaneously without loss of charge.

This reset/replenishment transition pulse is used to capture and store the present time of a local clock within one ASIC. This changes the basic quantum of information for each pixel from the traditional charge-per-unit-of-time data format to the difference between one clock capture and the next sequential capture, that is, the reset time difference (RTD). This new unit of information measures the time to integrate a predefined charge (ΔQ). Physics signals will produce a sequence of short [$\mathcal{O}(\mu s)$] RTDs. In the absence of a signal, the quiescent input current from backgrounds (^{39}Ar, cosmogenic, and other radioactivity) would be small, and the expected RTDs are on the order of seconds.

Signal waveforms can be reconstructed from RTDs by exploiting the fact that the average input current and the RTD are inversely correlated ($I \propto 1/\text{RTD}$), where I is the average current over an interval ΔT, and thus $I \cdot \Delta T = \int I(t)\,dt = \Delta Q$. The signal current is captured with fixed ΔQ (determined by the charge integrator/reset circuit) but with varying time intervals. The target ΔQ for the Q-Pix readout is between 0.3 and 1.0 fC of charge (corresponding to ~295 keV of deposited energy). This architecture of Q-Pix makes the time at which a reset occurs the fundamental quantum of information.

Simulations of Q-Pix have shown that this architecture can enhance the physics capabilities of large-scale LArTPCs through its ability to have a low-threshold, high-granularity readout. The first of these demonstrations showed the improved reconstruction enabled by a pixel-based

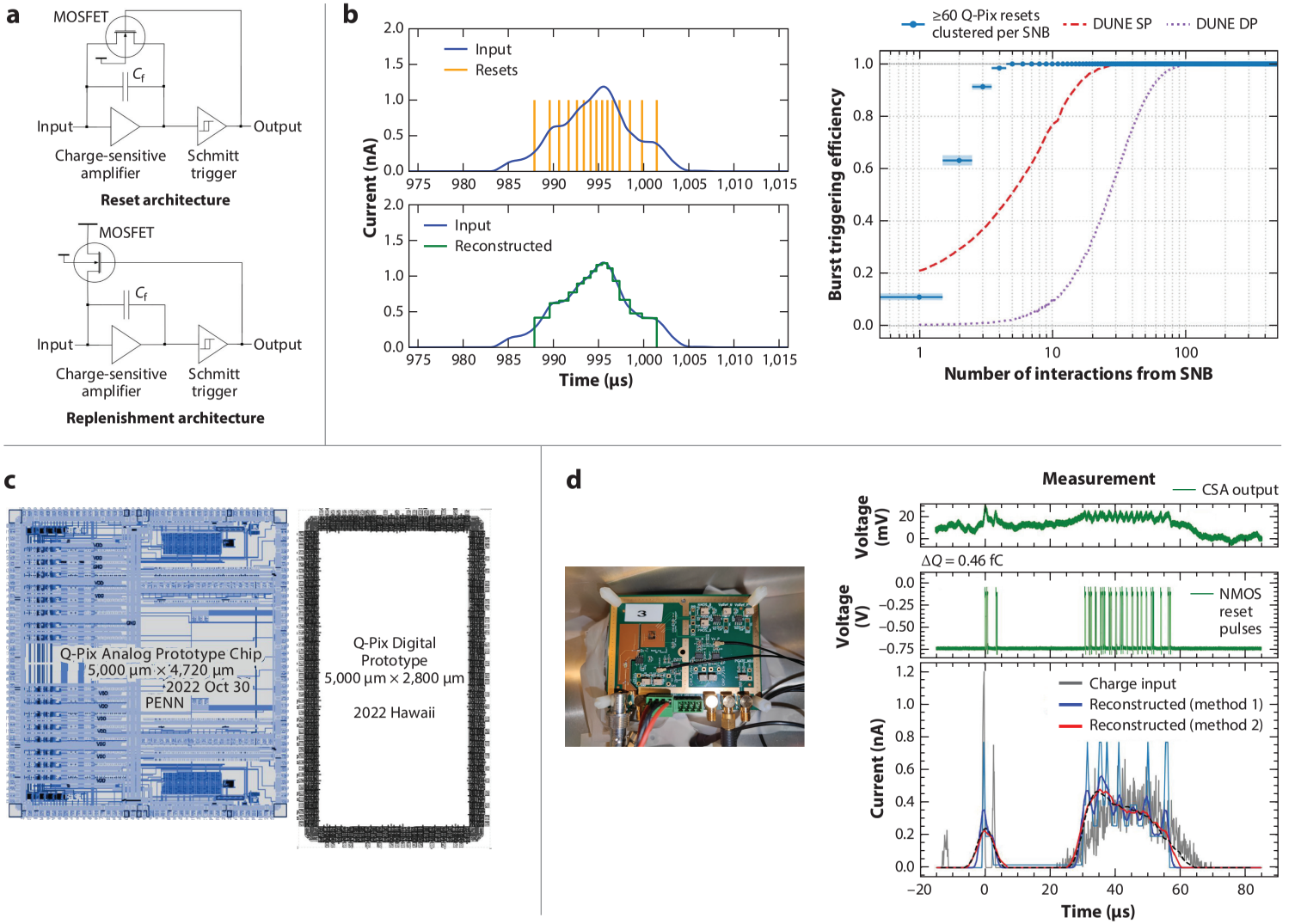

(*Caption appears on following page*)

Figure 5 (*Figure appears on preceding page*)

(*a*) Schematic overview of both the reset (*top*) and replenishment (*bottom*) architecture for the Q-Pix readout. (*b*) Simulation results of the Q-Pix readout. (*Left*) An example input waveform (*blue*) and corresponding time-stamped reset/replenishment intervals (*orange*). The reconstructed input waveform can be seen in green. (*Right*) The simulated SNB triggering efficiency for a Q-Pix–instrumented 10-kiloton LArTPC as a function of the number of recorded neutrino interactions. The Q-Pix efficiency for identifying an SNB is estimated to exceed that of traditional technologies. Panel adapted from Reference 55 (CC BY 4.0). (*c*) Schematics of the Q-Pix analog and digital ASICs submitted for fabrication in 2022. (*d*) (*Left*) An image of the discrete component circuit inside a shielding box. (*Right*) Current waveform reconstructed using a discrete-component implementation of the Q-Pix replenishment scheme. Abbreviations: ASIC, application-specific integrated circuit; CSA, charge-sensitive amplifier; DP, dual phase; DUNE, Deep Underground Neutrino Experiment; LArTPC, liquid argon time-projection chamber; SNB, supernova burst; SP, single phase.

detector compared with a projective-based readout for multi-GeV neutrino interactions (such as those that would be seen in future long-baseline experiments like DUNE) (33). This analysis showed enhanced efficiency and purity across all neutrino interaction types analyzed and the ability to reconstruct the topology and hadronic content (including the number of final-state protons and charged and neutral pions). Moreover, through an analysis of supernova neutrino interactions and a simulation of the Q-Pix architecture, it was shown that Q-Pix can significantly enhance the low-energy neutrino capabilities for kiloton-scale LArTPCs. Specifically, Q-Pix (*a*) enhances the efficiency of reconstructing low-energy supernova neutrino events over the traditional wire-based readout, (*b*) allows for a high-purity and high-efficiency identification of supernova neutrino candidates, (*c*) affords these enhancements at data rates 10^6 times less for the same energy threshold, and (*d*) allows for supernova burst pointing accuracy of <20 degrees from a single 10-kiloton module.

A number of prototypes are currently under construction and evaluation to demonstrate the Q-Pix readout architecture. These include designs in both 180- and 130-nm CMOS technology, evaluation of the architecture using discrete commercial-off-the-shelf components (COTS), and extensive digital prototyping using field-programmable gate arrays.

The 130-nm design implements the basic reset architecture via a simple analog integrator (25 mV fC^{-1}), comparator, and NMOS reset transistor. This design was done in the open-source Skywater package (**https://github.com/google/skywater-pdk**) and was not optimized for power consumption; instead, its design is focused on demonstrating the functionality and thus is estimated to consume ∼75–150 μW per channel. The 180-nm design consists of a 16-channel analog chip with the replenishment architecture implemented and a 16-channel digital chip, and both are optimized to lower the power consumption of the chips. The analog chip contains eight standard gain channels and eight C-gain (capacitor-based gain) channels. Each bank of eight channels has its own services, including serial interface, ring oscillator, power-on reset, and calibration circuit. Each standard gain channel consists of an analog integrator (20 mV fC^{-1}), an intermediate amplifier (×3), a comparator, and a programmable replenishment circuit and is estimated to consume ∼45 μW per channel. C-gain channels have the same functionality but use a different analog integrator with much higher gain (48 mV fC^{-1}) to avoid the need for an intermediate amplifier. This reduces unknown offsets, reduces internal delay and power, and allows a wider range of bandwidth versus intrinsic noise. The C-gain channels have a power consumption estimated to be ∼25 μW per channel. The digital chip contains 16 differential inputs, digital memory (local and global buffers), and a ring oscillator and implements the ENDEAVOUR readout protocol with LVDS output. The layout of the chip is shown schematically in **Figure 5*c***.

Figure 5*d* shows the implementation of replenishment architecture for the Q-Pix readout done using COTS discrete components. This prototype was able to demonstrate the fidelity of reconstructing input from an arbitrary waveform generator with a replenishment threshold of 0.46 fC, replenishment pulse widths of ∼300 to 600 ns, and linear responses to replenishment up to rates of 2 MHz. This demonstration provides confidence that the architecture proposed will

be capable of meeting the performance needs of future large-scale LArTPCs. The consortium of universities and labs working on this project expects both small- and large-scale demonstrations [$\mathcal{O}$(1,000–100,000) pixels] in LArTPCs in the next few years.

4.3. Amplifying Detectors

Another avenue that has been pursued is to amplify the ionization charge signal by using other physical methods before it reaches the detector electronics. This can be accomplished in a number of different ways, each of which has benefits and trade-offs. Different techniques currently being explored are described in the subsections below.

4.3.1. LArCADe. Single-phase LArTPCs have demonstrated their capability to capture signals at the MeV scale and above with a primary focus on neutrinos within the GeV energy range. The Liquid Argon Charge Amplification Device (LArCADe) (56) program aims to leverage altered anode geometries to amplify the amount of charge collected through gain in the liquid near the charge collection anode. This work builds on earlier pioneering work done with small additives to stabilize the gain achieved (57). This approach seeks to harness electron avalanches and thereby lower the detection thresholds. By doing so, it can extend the dynamic range to allow single-phase LArTPCs to be sensitive to phenomena like coherent elastic neutrino–nucleus scattering and the quest for dark matter such as weakly interacting massive particles. One such example of early work that shows promise is the implementation of thin, tip-like structures near the anode to amplify the electric field in a localized region. Simulations show that for tip heights of 3.5 mm and an apex radius between 10 nm and 1 μm, charge multiplication between 2 and 10 times is achievable with a bulk electric field between 500 and 1,000 V cm^{-1} (56).

Achieving stable and linear charge gain is an essential component to reconstruct the energy of the ionizing particle with high fidelity. To this end, a Monte Carlo package known as TRANSLATE (Transport in Liquid Argon of Near-Thermal Electrons) has been developed to simulate the transport of electrons in argon over a broad range of electric field strengths (58). In addition to this simulation work, initial prototyping of different submicrometer-scale tip geometries located near the anode to enhance the electric field has shown some promising preliminary results.

4.3.2. Dual-phase time-projection chambers. An alternative method to amplifying the ionization charge created in a LArTPC is to drift the electrons vertically toward the liquid–gas interface and extract the electrons from the liquid into the gas. Charge amplification is then possible in the argon vapor by large-area LEMs (large electron multipliers) and collected on an anode plane with a strip readout. LEMs are typically millimeter-thick PCBs with submillimeter-sized holes and two independently conductive surfaces. This allows for a high-electric-field area inside the holes, which enables large charge multiplication in a device that is mechanically robust and compatible with a cryogenic environment. The charge gain possible in the gas phase can be made very linear and uniform. This method of charge amplification enables, in principle, the construction of giant LArTPCs with drift lengths >10 m without deteriorating its imaging performance.

The genesis of dual-phase LArTPCs can be traced back to the pioneering experiments ZEPLIN-II and ZEPLIN-III in the early 2000s, which harnessed xenon-based dual-phase technology for dark matter searches (59, 60). These experiments set the stage for subsequent developments, including the Liquid Underground Xenon (LUX) (61) and LUX-ZEPLIN (62) experiments and the abovementioned argon-based dual-phase experiments such as WArP, MiniClean, DEAP, and DarkSide (63).

At the heart of dual-phase LArTPCs is the implementation of Townsend multiplication. Townsend multiplication is the process by which free electrons have sufficient mobility in the presence of an electric field to create secondary ionization via their impact. The positive ions, having a larger mass and lower mobility, do not contribute to the multiplication process, and there is a resulting avalanche of electrons from the initial state. In dual-phase TPCs, this is facilitated by a micropattern detector known as the Thick Gas Electron Multiplier (THGEM). This device, which represents an advancement of gas electron multipliers (GEMs), leverages an insulating layer with conductive surfaces to create extraction and amplification fields, leading to electron multiplication and secondary scintillation light production.

This technology has seen much success in the context of direct dark matter searches and is culminating in the deployment of a multikiloton dual-phase LArTPC as part of the Global Argon Dark Matter Collaboration (GADMC) program. These detectors will use underground argon that is depleted of radiological backgrounds to enhance the sensitivity of searches for dark matter (64).

The implementation of dual-phase LArTPCs has also seen extensive prototyping happening within the context of the DUNE experiment when considering the implementation of a dual-phase module (referred to as DUNE-DP). Demonstrations of the dual-phase readout were shown at TPC scales ranging from $10 \times 10 \times 21$ cm (approximately 3 kg of liquid argon) up to $6 \times 6 \times 6$ m (approximately 1 kiloton of liquid argon). Many technical challenges were faced at this large scale. In particular, instabilities of the extraction fields that pull the electrons from the liquid into the gas phase posed risk to the long-term stability of the experiment. Variability in the liquid level relative to the amplification device over many meters led to gain variation across the detector. Moreover, during operations of the 6 m × 6 m × 6 m dual-phase TPC, the THGEMs experienced sparking instabilities. Because a dual-phase TPC has only one anode, which is located at the top of the detector in the gas phase, the cathode must be placed near the bottom of the TPC. This single drift volume requires a higher cathode potential than would be necessary for multiple anodes, and it proved technically difficult to achieve at the 12-m distances needed for DUNE. As of the writing of this manuscript, the DUNE Collaboration has concluded the R&D into the dual-phase readout and deemed the technology not yet sufficiently mature to proceed as a detector option for the project (65).

However, other techniques to utilize the gain in the gas are still active areas of research (see Section 6.3).

4.3.3. ARIADNE. The ARIADNE technique leverages electroluminescence for optical readout of dual-phase LArTPCs (**Figure 6**) (66). After drifting electrons are extracted to the gas phase, they pass through a THGEM with 0.5-mm holes at 0.8-mm spacing (67). Acceleration of electrons in the holes in the GEM excites argon atoms, which then emit ∼100 photons per primary electron. A plate coated with tetraphenyl butadiene (TPB) located above the THGEM converts these vacuum ultraviolet (VUV) photons to the visible spectrum. Custom optics are used to view a large area [$\mathcal{O}(1)$ m^2] of the wavelength-shifting plate. An image intensifier is used to further amplify the optical signal. A TimePix-based camera, with 256×256 pixel resolution, 10-bit intensity measurement, and 1.6-ns time resolution, is used to record the optical signals (68). A recent 2- by 2-m prototype of the ARIADNE system has successfully imaged cosmic rays in a ton-scale test cryostat at the CERN Neutrino Platform (69).

This technique has multiple advantages for readout of dual-phase LArTPCs. The optically based readout removes the need for cryogenic electronics and cabling, and it mitigates the introduction of electrical noise into the detector. The spatial resolution of the readout can be improved through the use of higher-resolution optics and cameras. The optics and camera are

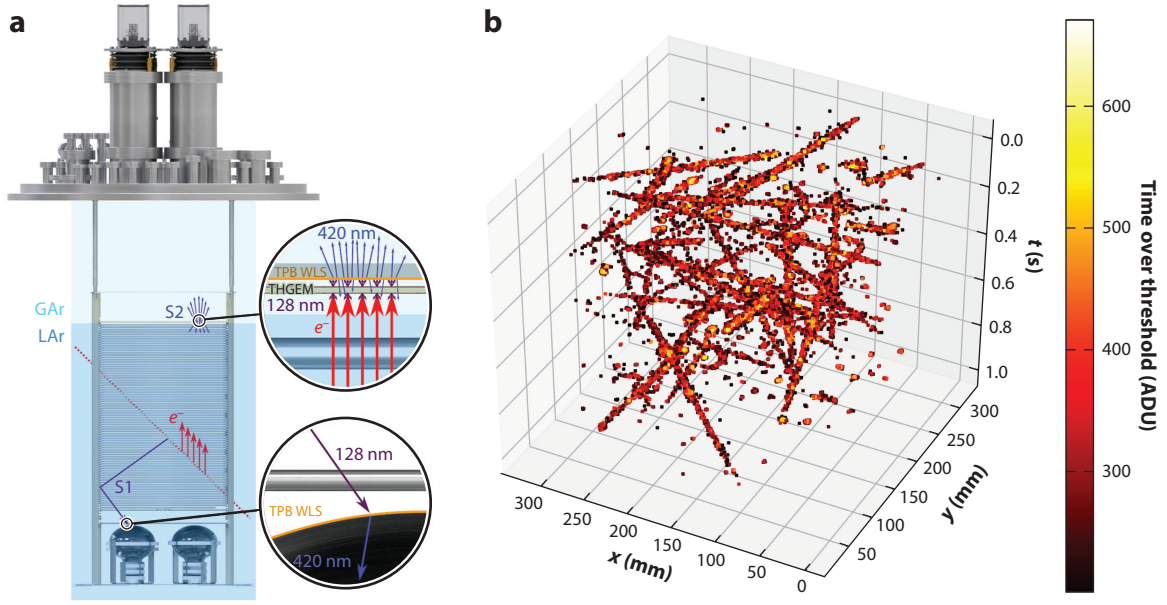

Figure 6

(*a*) Conceptual drawing of the dual-phase optical readout method of the ARIADNE prototype. The primary scintillation light (S1) is detected using TPB-coated photomultipliers, while the electroluminescence generated in a THGEM (S2) is converted by a TPB-coated plate and imaged using a fast optical camera. (*b*) An overlay of 1 s of data collected during prototype operation, primarily consisting of cosmic-ray track segments. Abbreviations: ADU, analog-to-digital unit; GAr, gaseous argon; LAr, liquid argon; THGEM, Thick Gas Electron Multiplier; TPB, tetraphenyl butadiene; WLS, wavelength shifter. Figure adapted from Reference 66 (CC BY 4.0).

located outside the cryogenic environment, easing maintenance and upgrades. Development of direct imaging of the VUV photons is a future step in the ARIADNE program.

5. DEVELOPMENTS IN SCINTILLATION PHOTON DETECTION

Detection of VUV liquid argon scintillation photons is commonly used for triggering, fine-timing, and calorimetry. Relative to the ionization signal, which is delayed by electron drift to anode sensors, the scintillation signal is prompt and provides the reference time of interaction with a precision of $\mathcal{O}(1)$ ns. The scintillation signal is complementary to the ionization signal and provides an additional handle to enhance calorimetric energy resolution.

For applications at energies of $\mathcal{O}(1)$ GeV in very large detectors (e.g., accelerator neutrino experiments), scintillation light is primarily used to trigger the detector and define the start time of electron drift (30, 70, 71). This can be achieved with photon detection systems with low collection efficiencies, typically $\mathcal{O}(10^{-4})$. Triggering for rare event searches at MeV energies and below requires higher efficiencies that are achieved through a combination of increased photocoverage as well as the use of high-reflectivity materials such as polytetrafluoroethylene in relatively smaller noble liquid TPCs (72–74). The increased photon collection efficiency improves the detector energy resolution as well as the background rejection via the time profile of scintillation emission and the ionization-to-scintillation ratio. Much of the recent R&D has been focused on technologies to increase photon collection efficiencies for very large ($\gg$1 ton) future detectors. Lower-energy (75, 76) applications (<100 MeV), such as supernova neutrino (77, 78), solar neutrino (79), and dark matter direct detection (42, 64, 80, 81), have stringent requirements on light response uniformity

and detection efficiency. Increased efficiency, combined with detector optical segmentation, is also being explored to enable the use of LArTPCs in high-rate environments (51) to enhance interaction-level assignment of final-state particles to their respective originating interactions.

5.1. Light Traps

Light traps (82–85) enhance photon collection efficiency by funneling photons to a smaller active photosensor area. For multikiloton LArTPCs with surface areas >100 m^2, scintillation direct detection with photomultiplier tubes (PMTs) or silicon photomultipliers (SiPMs) is impractical.[3] To increase collection efficiency, wavelength shifters (WLSs) (87) are commonly used to downshift the VUV liquid argon scintillation to visible wavelengths before detection. For example, experiments like DarkSide (88) and SBND (70) have opted to coat PMT entrance windows and TPC inner surfaces with wavelength-shifting material to enhance both light detection efficiency and detector response uniformity.

The ARAPUCA technology pioneered an efficient light-trapping technique using dichroic filters that are highly transparent to wavelengths below a cutoff value and highly reflective to wavelengths above this cutoff value. The ARAPUCA device is composed of a low-profile box cavity immersed in liquid argon with highly reflective internal walls. The detector face consists of a dichroic filter entrance window with a *para*-Terphenyl WLS on the external box side for downshifting VUV scintillation photons to 350 nm and wavelength-shifting material on the internal-box side for downshifting photons from 350 to 430 nm. An enhanced version of this light-trapping device, dubbed X-ARAPUCA (89), features an acrylic slab—the EJ-286PS model manufactured by Eljen Technology (90)—with a WLS embedded within. A prototype X-ARAPUCA and a diagram depicting the working principle are shown in **Figure 7*a*,*d***. SiPM photosensors are coupled to an edge of the WLS acrylic slab. Photons are funneled to SiPMs by either total internal reflection within the acrylic slab or reflection from the internal side of the dichroic filter. X-ARAPUCAs sized at 9.6 × 12.5 cm have demonstrated ∼2% absolute photon detection efficiency (PDE) (91) in liquid argon. Roughly 6,000 X-ARAPUCA units, each 480 × 93 mm^2, will be used in the first 10-kiloton DUNE Far Detector (92).

Two trap technologies have been prototyped for the DUNE Near Detector LArTPC (51), the ArCLight (93), and the Light Collection Module (LCM) (94). **Figure 7** shows schematics describing the working concepts for the LCM (**Figure 7*b***) and ArCLight (**Figure 7*c***) alongside images of the LCM (**Figure 7*e***, *top*) and ArCLight (**Figure 7*e***, *bottom*) instrumented prototypes. The basic operation principle is shared among the two devices. TPB is coated on the outer surface of each light trap, downshifting VUV scintillation photons to ∼430 nm. Visible photons within the light trap device are then downshifted further to green light by a bulk structure infused with a coumarin dopant. Similarly to the X-ARAPUCA, the ArCLight design relies on a dichroic film to prevent escape of the green light. The LCM trap relies on total internal reflection of WLS-doped optical fibers. SiPMs couple to the edge of each light trap. In the first large-scale prototype demonstration, LCM devices demonstrated an average PDE of ∼0.6%, and ArCLight devices demonstrated an average PDE of ∼0.2% (95).

5.2. LightPix

LightPix is designed to provide a low-power, cryogenic-compatible SiPM readout system that can scale to $>10^6$ channels. To achieve this it shares much of the same design with the LArPix pixelated readout system that has already been demonstrated at this scale (see Section 4.2.1).

[3]Notwithstanding, significant progress has been made to produce large-surface-area [$\mathcal{O}(100)$ cm^2 per unit] SiPM systems (86). As such, tileable large-area SiPM readout may be realizable in the near future.

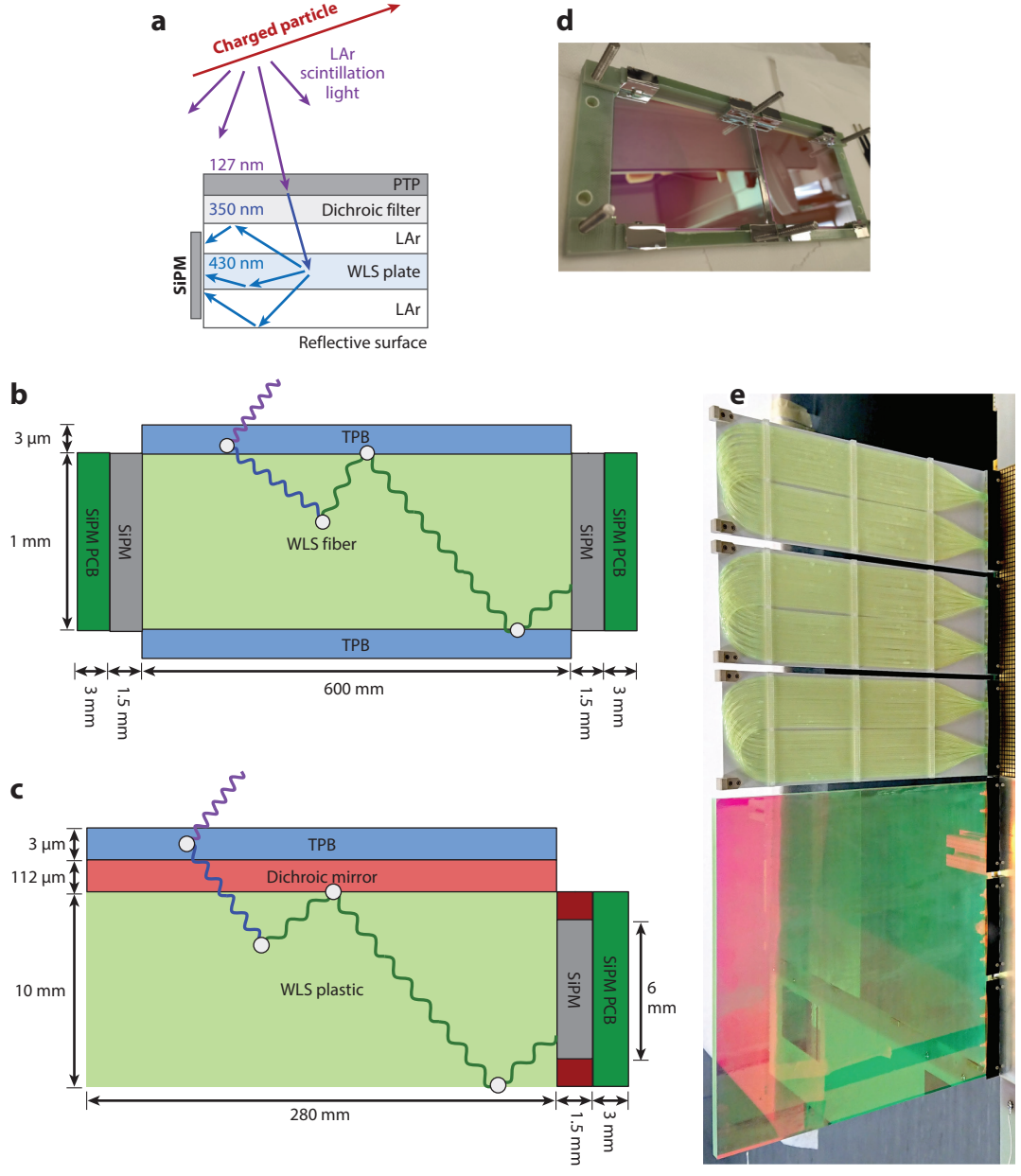

Figure 7

Light-trapping and detection concepts for the (*a*) X-ARAPUCA, (*b*) LCM, and (*c*) ArCLight light traps. (*d*) An X-ARAPUCA prototype with two dichroic windows, where the overall area measures 200 × 75 mm^2. Four photosensor boards (each containing four 6 mm × 6 mm SiPMs in parallel) are coupled to the WLS-doped acrylic slab. Panels *a*–*d* adapted from Reference 90 (CC BY 4.0). (*e*, *top*) Three LCM light traps, each with dimensions of 10 × 100 × 300 mm, and (*bottom*) an ArCLight light trap with dimensions of 10 × 300 × 300 mm, as instrumented in the DUNE LArTPC Near Detector prototype. Panel adapted from Reference 53 (CC BY 4.0). Abbreviations: LAr, liquid argon; LArTPC, LAr time-projection chamber; LCM, Light Collection Module; PCB, printed circuit board; PTP, *para*-Terphenyl; SiPM, silicon photomultiplier; TPB, tetraphenyl butadiene; WLS, wavelength shifter.

The LightPix-v1 ASIC is implemented in 180-nm CMOS technology as a mixed-signal integrated circuit. The detector readout system-on-a-chip ASIC contains 64 analog channels, each composed of a low-power CSA, a discriminator with a programmable threshold, and a time-to-digital converter (TDC). The TDC is composed of a ramp generator coupled to an 8-bit SAR ADC with a least significant bit at a nominal value of 0.5 ns. It provides a fine-timing measurement capturing the time difference between the discriminator crossing and the next 10-MHz system clock rising edge. The ASIC digital core assembles an event record of each trigger noting the TDC value, threshold-crossing time (a 10-MHz coarse timing measurement), and channel and chip unique identifiers. Pseudodifferential signal I/O is implemented, leveraging the dynamic and versatile Hydra I/O scheme originally designed for LArPix.

Dark count suppression is a key feature of the LightPix-v1 ASIC design and can be achieved at two levels in the system. The single-channel threshold may be set above the level of the single photoelectron signal, suppressing the bulk of dark counts. Alternatively, dark counts can be suppressed at the chip-wide (64-channel) level using multichannel coincidence logic available in the ASIC digital core. If a specified number of channels are above threshold within a tunable time window, then the chip records the data. For cryogenic applications, both the SiPM and the LightPix ASIC are operated in the cryogenic medium, naturally reducing the dark count rate and electronics noise.

The LightPix-v1 ASIC was designed for use in very-high-channel-count systems with low occupancy, where the typical number of photons per channel is less than one. For this reason, it does not record signal amplitude. Calorimetry and pulse-shape discrimination are instead achieved through the aggregate distribution of photon arrival times across many SiPMs. LightPix-v1 is in effect a single photoelectron discriminator with a TDC for fine-timing.

Subnanosecond timing accuracy has been demonstrated when self-triggering on externally injected signals of single-photoelectron amplitude. The LightPix TDC linearity has been measured by sweeping an external delay (provided by a delay generator) across the full 100-ns timing range in 5-ns increments in self-triggering mode. At delays greater than 10 ns from the ramp generator start, the TDC is linear to within 2%. Within 10 ns of the ramp generator start, the TDC is linear to within 10%. At channel thresholds as low as ~5,000 electrons, <2-ns slew rate and <1-ns jitter were measured with charge injection tests. A prototype LightPix system has been used in combination with VUV-sensitive 3 mm × 3 mm Hamamatsu S13370-3075CN SiPMs to detect cosmic rays in high-purity liquid argon.

Continued LightPix development is focused in three areas: front-end optimization for SiPMs (6 mm × 6 mm or larger), a variant that records signal amplitude for use at higher occupancies (>1 photoelectron per channel), and development of a tileable multi-SiPM unit with integrated readout. LightPix is envisioned to be a general multipurpose, high-channel-count light readout unit that can serve as an effective alternative to PMTs.

5.3. Signal-over-Fiber and Power-over-Fiber

To increase the overall photocoverage in a LArTPC, one idea that has been considered is to embed these devices within the high-voltage cathode and field cage. Such a deployment could begin to approach 4π coverage of the interaction and greatly enhance the light collection efficiency of the detector. One challenge of this integration scheme is that the power and analog readout of the photon detectors needs to be done through a nonconductive material as the environment is at $\mathcal{O}(-100)$ kV. A proposed solution is to use power-over-fiber (PoF) and signal-over-fiber (SoF) for the light detectors.

PoF and SoF have been studied in the context of the X-ARAPUCA technology for DUNE (96) as described in Section 5.1. The SoF technique begins with a multistage amplification of the

SiPMs' differential signal. Initially, it is amplified with a gain of approximately five and subsequently converted into a unipolar signal at the second amplification stage, which provides a gain of about two (resulting in a total gain of approximately 20 times). This signal is then directed to the third stage, which is a laser driver responsible for controlling the current of a 1,310-nm Fabry–Pérot diode laser. The laser is maintained with a constant offset to ensure that it remains within its linear operating range. To enable this system to operate both in liquid argon and at room temperature, a set of parallel resistors and a negative-temperature-coefficient thermistor are employed. The analog signal is then transmitted via an optical fiber to a warm receiver, where it is converted back into an analog electrical signal that can be digitized by the data acquisition system.

PoF is accomplished through the use of GaAs photovoltaic power converters. Each receiver can output up to 7 V and to a maximum current of ~80 mA. This configuration allows a higher current output for the active components and the DC-to-DC converter, which is around 100 mA. The GaAs alternative was chosen due to the high conversion efficiency (>50%) even in liquid argon. The input light is provided by a Broadcom module with an 808-nm laser diode capable of delivering +2 W through a standard multimode fiber link (62.5/125 μm).

Recently, an array of SiPM-based photon detectors (X-ARAPUCAs) was successfully powered using PoF and read out with SoF at the CERN Neutrino Platform. The performance of the SoF gave a signal-to-noise-ratio >4 and allowed for single-photoelectron calibration via a low-intensity ultraviolet LED (96). This technology is planned for use in a DUNE Far Detector with ongoing R&D to improve performance.

6. DEVELOPMENT OF INTEGRATED ELECTRON AND PHOTON DETECTION

Another approach to increase photocoverage and detection efficiency is to combine charge and light detection into a single integrated sensor, thus allowing the charge collection anode to also include sensitivity to scintillation light. Such a new detector element would (*a*) provide intrinsic fine-grain information for both ionization and scintillation, opening up new exciting possibilities to exploit the imaging capabilities of both signals, (*b*) enhance the amount of light collected through increased surface area coverage, and (*c*) simplify the design and operation of noble element detectors. Different approaches to realize such a sensor are described below. The first uses photoconductive materials integrated into the pixel-based readout plane (Section 6.1), the second repurposes the same charge readout electronics to readout arrays of VUV-sensitive SiPMs embedded in the pixel-based readout (Section 6.2), and the third converts the charge to light through a novel in-situ dual-phase approach (Section 6.3).

6.1. Q-Pix (Photons)

One method being pursued to realize an integrated charge and light sensor is to coat a pixel-based charge readout with a type of photoconductive material that, when struck by an ultraviolet photon, would generate a signal (charge) that could be detected by the same charge readout scheme considered for the ionization charge. This idea is shown schematically in **Figure 8*a***. With the proper choice of photoconductor, such a device could have a broad frequency response and thus detect the full spectrum of light produced in noble element TPCs from VUV to visible wavelengths.

Three such photoconductive materials have been explored in recent R&D: (*a*) amorphous selenium (aSe) (97), (*b*) ZnO (98), and (*c*) organic photodiodes (OPDs) (99). Their application in a liquid argon environment is currently under investigation.

aSe is attractive because it has been extensively studied in the context of medical imaging devices for its application in X-ray detection (and thus can be manufactured over large areas at

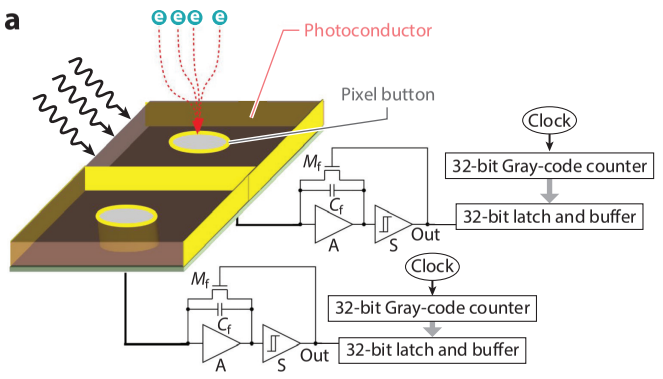

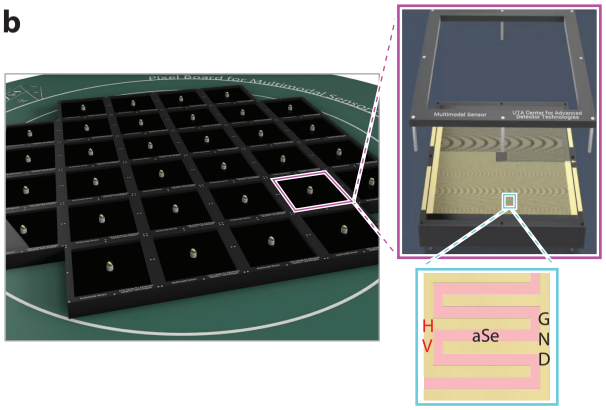

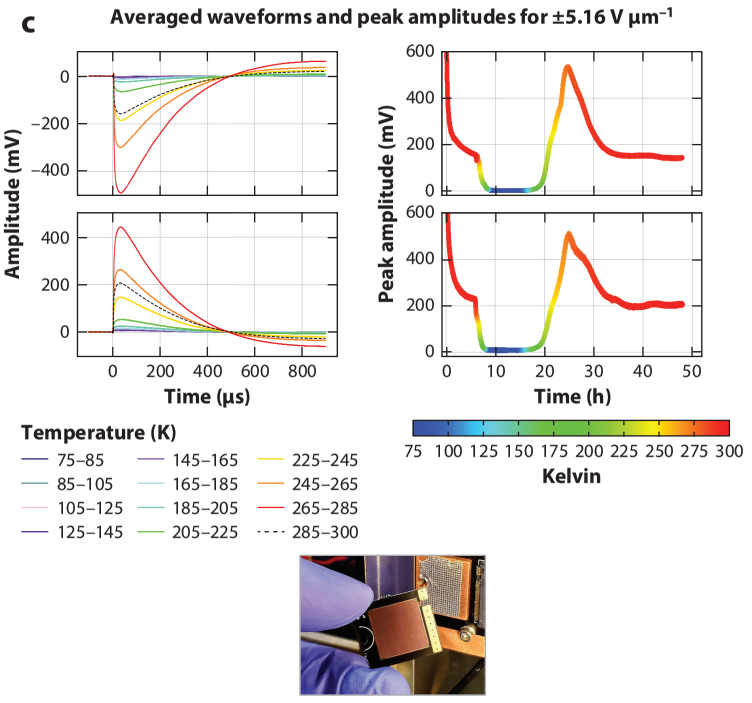

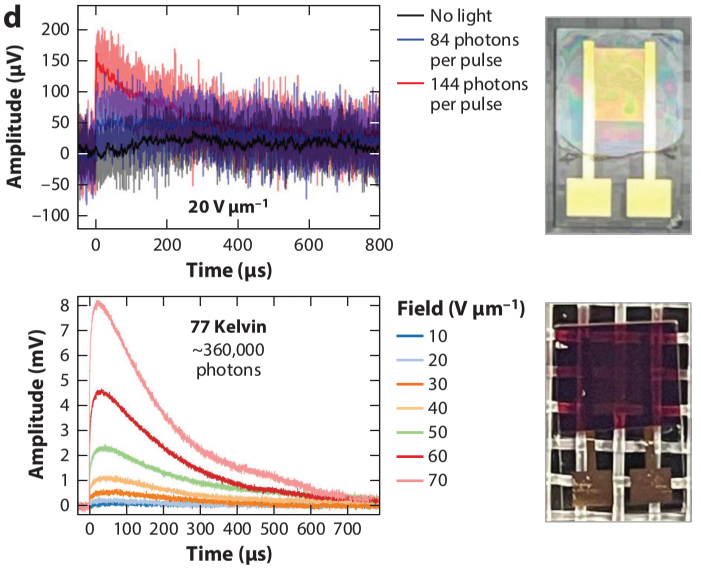

(Caption appears on following page)

Figure 8 (*Figure appears on preceding page*)

(*a*) Conceptual sketch of an integrated Q+L sensor. This device would use the same readout architecture that is used for the detection of ionization charge to detect the charge from the photoconductor. Panel adapted from Reference 100. (*b*) Engineering sketch of a multipixel Q+L sensor implementing an IDE structure and adapted into a pixel-based readout anode. (*c*) First demonstration of a windowless aSe-based detector's response to VUV light as a function of temperature between 77 and 290 K in the collection of both holes and electrons; the device is shown in the inset. Graphs adapted from Reference 100. (*d*) Recent progress on the windowless aSe detector concept at smaller IDE pitch showing the response to $\mathcal{O}(100)$ photons in a low-IDE field and the gain achieved in a higher-IDE field at cryogenic temperatures for a larger flux of photons. Abbreviations: aSe, amorphous selenium; GND, ground; HV, high voltage; IDE, interdigitated electrode; Q+L, charge plus light; VUV, vacuum ultraviolet.

high quality and low cost). It has a high absorption coefficient at VUV wavelengths while simultaneously being sensitive to light at wavelengths between 400 and 500 nm for relatively thin coatings. Additionally, aSe has the ability to achieve high internal gain and thus produce currents compatible with cryogenic charge readout.

Similarly, the performance and manufacturing techniques of ZnO have been extensively studied for photovoltaic and photon detectors across the entire range of wavelengths. ZnO has a stable response at cryogenic temperatures and can be doped with other materials to customize wavelength sensitivity, thus providing an avenue for a wavelength-specific response. When mated with other material surfaces, it can form a Schottky barrier diode and thus enhance the signal from the absorption of a photon through low-voltage electron pair generation from the band-to-band excitation; it also can enhance the response speed of the device.

Of all the options for photoconductive materials, OPDs have probably the largest existing knowledge base in manufacturing since they are used in additive manufacturing, solar energy applications, and the organic LED photosensors found in commercial devices (e.g., electronic screens). The manufacturing is relatively simple and low-cost (done through roll printing and/or spin coating) and can be applied to rigid or flexible surfaces. However, despite these advantages, their application to VUV light in a cryogenic environment is largely unknown, and additional R&D is required to overcome their relatively slow response time of $\mathcal{O}(0.5–5)$ μs.

Initial studies regarding construction of a multimodal pixel detector have focused on using aSe due to the ease of prototyping and testing. Designs for a multimodal pixel are shown in **Figure 8*b***, in which an interdigitated electrode (IDE) is deposited around the central ionization collection pixel. This design provides a straightforward way to apply a local electric field to the aSe and enable charge gain as well as to instrument the area between the charge collection pixels. **Figure 8*c*** shows results from the first study of this design, which was done on a small scale on commercially manufactured PCBs (100). This study showed the viability of an IDE-based aSe device at cryogenic temperatures with a response to VUV photons. More recent studies have pushed this capability further to characterize the performance of such a design with a low flux of photons [$\mathcal{O}(100)$ photons], at high electric fields (>70 V μm^{-1}), and at cryogenic temperatures. These results continue to show promise, and further R&D regarding aSe-based devices (as well as other photoconductors) is anticipated to be an area of active research in the near future.

6.2. SoLAr

The SoLAr program also aims to develop a pixelated anode that is sensitive to both ionization electrons and scintillation photons (79). The concept is to develop a custom silicon sensor that integrates both charge-sensitive pixels and VUV photon sensitivity, akin to SiPMs, in a single sensor (**Figure 9**). Since work on the custom sensor is a longer-term effort, in the interim the SoLAr team has developed a conceptual version using available components. In this version, VUV-sensitive SiPMs are interspersed over ∼10% of the area of a LArPix-based pixelated anode. This arrangement trades some distortion in the imaging of the ionization electron distribution for

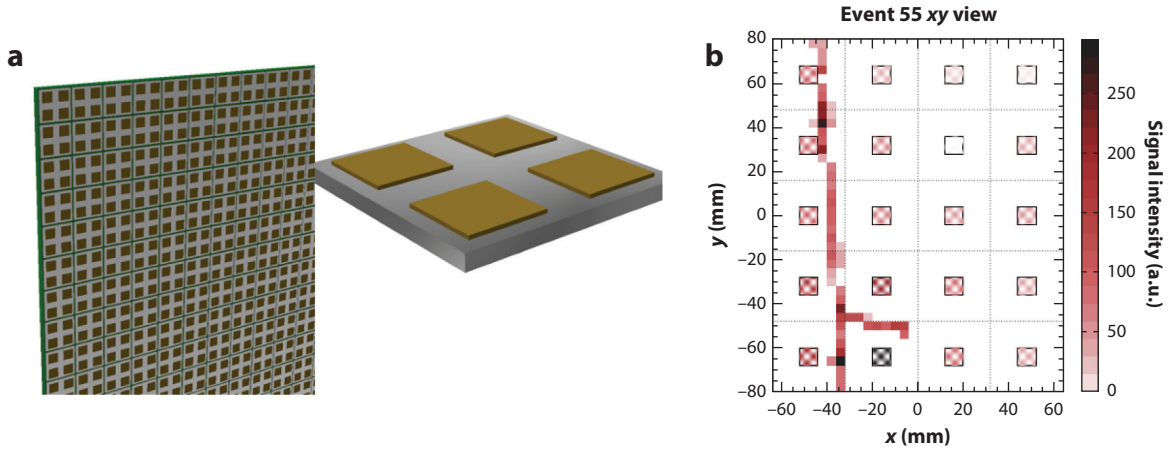

Figure 9

(*a*) Conceptual image of a SoLAr tile composed of multiple silicon-based elements sensitive to both scintillation photons and ionization electrons. Panel adapted with permission from Reference 79. (*b*) An example cosmic ray imaged using charge-sensitive pixel regions (*large squares*) surrounding VUV-sensitive SiPMs (*small central squares*) in a SoLAr prototype. Panel adapted from Reference 101 (CC BY 4.0). Abbreviations: SiPM, silicon photomultiplier; VUV, vacuum ultraviolet.

modest sensitivity to scintillation light. This has been realized in a small-scale (∼30 L) LArTPC and has been used to image cosmic rays.

6.3. Bubble-Assisted Liquid Hole Multipliers

The bubble-assisted liquid hole multiplier (LHM) is an innovative concept designed for simultaneous detection of ionization electrons and primary scintillation photons in noble liquids (102). The design consists of a perforated electrode, such as a GEM or THGEM, submerged within the liquid. Beneath the electrode, a bubble of noble gas of radius $\mathcal{O}(100)$ μm is carefully trapped. Optionally, the upper surface of the electrode is coated with a VUV-sensitive photocathode (e.g., a CsI photocathode). To generate and maintain the bubble, heating elements (such as a plane of heating wires) are located beneath the electrode. Once formed, the bubble resides below the electrode, remaining stable as long as the system is in a thermodynamic equilibrium; the buoyancy pushes it upward while the surrounding walls keep it confined from the sides.

Bias voltages are applied between the upper and lower surfaces of the electrode, as well as the heating wires, generating a dipole-like field within the holes of the electrode and a transfer field between the bottom of the electrode and the wire plane. The drift field above the electrode is established by the potential difference between the top surface of the electrode and a remote drift electrode (cathode plane) positioned above it.

Within the liquid, particle interactions result in an immediate scintillation signal (S1) and the emission of ionization electrons. These electrons migrate toward the LHM and are guided by the local field into the holes. Once they traverse the interface between the liquid and the bubble, they stimulate electroluminescent light (S2) within the gas, primarily in the high-field area near the bottoms of the holes. Similarly, S1 photons that strike the photocathode release photoelectrons. These photoelectrons are directed into the holes of the LHM, giving rise to an electroluminescent light signal (S1). The timing of the S1 electroluminescent light signal varies depending on the specific electrode used; it occurs tens to hundreds of nanoseconds after S1 and typically well before S2 (which ranges from microseconds to milliseconds depending on the drift distance). Both the S1

and S2 electroluminescent light signals can be captured by a position-sensitive photon detector (e.g., an SiPM array) situated beneath the bubble, which enables precise reconstruction of their 2D location.

The operation of an LHM has been demonstrated and used to measure the energy spectrum of alpha particles from the decay of ^{241}Am with an energy resolution of 13.5% (103). There has been recent progress in the observation of bubbles and advances in bubble electrodynamics via numeric simulations (104). For the first time, groups were able to visually observe bubbles within liquid argon and measure their dynamic contact angles on potential materials used for LHM electrodes—namely, Cu, FR4, Teflon, and Kapton. These findings were further explored through numeric simulations to understand the impact of external electric fields on bubble equilibrium configurations and the liquid–gas interface, particularly when holes are present. One key observation is that electric fields near the interface act as an additional pressure factor affecting the equilibrium, resulting in a downward force and causing deformations in the bubble interface proportional to the applied field's intensity. Micro-computed-tomography imaging experiments confirm these simulations in room-temperature water and silicone oil.

Additionally, extensive small-scale prototyping for different types of electrodes has shown promising results in both liquid argon and liquid xenon, demonstrating PDE values >15%. A continued R&D plan for future large-scale dark matter detectors is underway to understand the details of the scintillation light timing profile as well as the electroluminescent photon yield in different configurations.

7. CONCLUSION

Recent developments in novel readout techniques for LArTPCs have shown significant progress as presented in this review. For single-phase LArTPCs, the development of multilayer strip-based anodes has improved the mechanical reliability and facilitated production for very large detectors. Pixelated readout shares these advantages while also providing native 3D imaging, mitigating ambiguities associated with the traditional 2D projective techniques. Leveraging amplification in argon, through the dual-phase design or more novel approaches, improves the low-energy ($\ll$MeV) performance of LArTPCs. Dual-phase detectors also allow for an entirely optical readout, and the use of THGEMs and fast optical cameras has recently enabled a highly granular optical readout.

Similarly, recent developments in novel scintillation light detection have seen rapid progress as covered in this article. Various solutions implementing light traps and WLS have seen large-scale prototype deployment with promising performance. New and novel approaches to integrate ionization charge and scintillation light readout into a single sensor have also seen significant R&D with planned implementation in various configurations in the near future. Novel readout techniques allow for the deployment of light-detecting devices in areas of the detector not previously possible. Additionally, new techniques to convert charge signals into light-based signals have also seen significant progress with promising R&D forthcoming.

DISCLOSURE STATEMENT

J.A., D.A.D., and B.R. receive funding from the US Department of Energy (DOE) to undertake work discussed in this review. J.A., D.A.D., and B.R. are members of the DUNE Collaboration and participate in the DUNE experiment, which benefits from techniques described in this review. B.R. is a collaborating developer on LArPix and LightPix technologies, which are featured in this review.

ACKNOWLEDGMENTS

The development of this review article was supported by grants from the US Department of Energy, Office of High Energy Physics. This manuscript has been authored by employees of Lawrence Berkeley National Laboratory under Contract No. DE-AC02-05CH11231 with the US Department of Energy. The US Government retains, and the publisher, by accepting the article for publication, acknowledges, that the US Government retains a nonexclusive, paid-up, irrevocable, worldwide license to publish or reproduce the published form of this manuscript, or allow others to do so, for US Government purposes.

LITERATURE CITED

1. Aprile E, Doke T. *Rev. Mod. Phys.* 82:2053 (2010)
2. Workman RL, et al. (Part. Data Group.) *Prog. Theor. Exp. Phys.* 2022:083C01 (2022); Workman RL, et al. (Part. Data Group.) Review of particle physics: 2023 update. *Particle Data Group*. **https://pdg.lbl.gov/2023/reviews/contents_sports.html** (2023)
3. Miyajima M, et al. *Phys. Rev. A* 9:1438 (1974)
4. Amoruso S, et al. *Nucl. Instrum. Methods A* 523:275 (2004)
5. Acciari R, et al. *J. Instrum.* 8:P08005 (2013)
6. Zhang A, et al. *Nucl. Instrum. Methods A* 1010:165491 (2021)
7. Doke T, et al. *Jpn. J. Appl. Phys.* 41:1538 (2002)
8. Kubota S, et al. *Phys. Rev. B* 17:2762 (1978)
9. Heindl T, et al. *Eur. Phys. Lett.* 91:62002 (2010)
10. Santorelli R, et al. *Eur. Phys. J. C* 81:622 (2021)
11. Segreto E. *Phys. Rev. D* 103:043001 (2021)
12. Babicz M, et al. *J. Instrum.* 15:C03035 (2020)
13. Walkowiak W. *Nucl. Instrum. Methods A* 449:288 (2000)
14. Shibamura E, Takahashi T, Kubota S, Doke T. *Phys. Rev. A* 20:2547 (1979)
15. Li Y, et al. *Nucl. Instrum. Methods A* 816:160 (2016)
16. Tegeler Ch, Span R, Wagner W. *J. Phys. Chem. Ref. Data* 28:779 (1999)
17. Shutt RP. *Bubble and Spark Chambers: Principles and Use*, Vol. 1–2. New York: Academic (1967)
18. Charpak G, et al. *Nucl. Instrum. Methods A* 62:262 (1968)
19. Bressani T, Charpak G, Rahm D, Zupancic C. *Track localization by means of a drift chamber*. Rep., CERN, Geneva. **https://cds.cern.ch/record/1221302** (1969)
20. Nygren D. *eConf* C740805:58 (1974)
21. Attie D. *Nucl. Instrum. Methods A* 598:89 (2009)
22. Willis WJ, Radeka V. *Nucl. Instrum. Methods* 120:221 (1974)
23. Fabjan CW. *Nucl. Instrum. Methods A* 360:228 (1995)
24. Rubbia C. Report CERN-EP-77-08, CERN, Geneva (1977)
25. Amerio S, et al. *Nucl. Instrum. Methods A* 527:329 (2004)
26. Rubbia C, et al. *J. Instrum.* 6:P07011 (2011)
27. Baudis L. *Phys. Dark Univ.* 4:50 (2014)
28. Dolinski MJ, Poon AWP, Rodejohann W. *Annu. Rev. Nucl. Part. Sci.* 69:219 (2019)
29. Anderson C, et al. *J. Instrum.* 7:P10019 (2012)
30. Acciarri R, et al. *J. Instrum.* 12:P02017 (2017)
31. Aguilar-Arevalo AA, et al. *Phys. Rev. D* 103:052002 (2021)
32. Acciarri R, et al. arXiv:1503.01520 [physics.ins-det] (2015)
33. Acciarri R, et al. arXiv:1601.05471 [physics.ins-det] (2016)
34. Adamowski M, et al. *J. Instrum.* 9:P07005 (2014)
35. Bromberg C, et al. *J. Instrum.* 10:P07015 (2015)
36. Adams DL, et al. *J. Instrum.* 15:P03035 (2020)
37. Acciarri R, et al. *J. Instrum.* 15:P04026 (2020)

38. Abi B, et al. *J. Instrum.* 15:P12004 (2020)
39. Chen H, Radeka V. *Nucl. Instrum. Methods A* 1045:167571 (2023)
40. Zani A. *Adv. High Energy Phys.* 2014:205107 (2014)
41. Rielage K, et al. *Phys. Procedia* 61:144 (2015)
42. Amaudruz PA, et al. *Phys. Rev. Lett.* 121:071801 (2018)
43. Agnes P, et al. *Phys. Rev. D* 98:102006 (2018)
44. Shockley W. *J. Appl. Phys.* 9:635 (1938)
45. Ramo S. *Proc. IRE* 27:584 (1939)
46. Adams C, et al. *J. Instrum.* 13:P07006 (2018)
47. Adams C, et al. *J. Instrum.* 13:P07007 (2018)
48. Sacerdoti S. *Proc. Sci.* NuFact2021:173 (2021)
49. Lantwin O. *Proc. Sci.* ICHEP2022:332 (2022)
50. Asaadi J, et al. *Instruments* 4:6 (2020)
51. Abed Abud A, et al. *Instruments* 5:31 (2021)
52. Dwyer DA, et al. *J. Instrum.* 13:P10007 (2018)
53. Abed Abud A, et al. (DUNE Collab.) arXiv:2403.03212 [physics.ins-det] (2024)
54. Nygren DR, Mei Y. arXiv:1809.10213 [physics.ins-det] (2018)
55. Kubota S, et al. *Phys. Rev. D* 106:032011 (2022)
56. Beever Z, Caratelli D, Fava A. Technical Report FERMILAB-POSTER-19-098-ND, Fermilab, Batavia, IL (2019)
57. Kim JG, et al. *Nucl. Instrum. Methods A* 534:376 (2004)
58. Beever Z, et al. *Comput. Phys. Commun.* 297:109056 (2024)
59. Alner GJ, et al. *Astropart. Phys.* 28:287 (2007)
60. Akimov DY, et al. *Astropart. Phys.* 27:46 (2007)
61. Akerib DS, et al. *Phys. Rev. Lett.* 112:091303 (2014)
62. Malling DC, et al. arXiv:1110.0103 [astro-ph.IM] (2011)
63. Bossa M. *J. Instrum.* 9:C01034 (2014)
64. Aalseth CE, et al. *Eur. Phys J. Plus* 133:131 (2018)
65. Marchionni A, Autiero D, Duchesneau D, Cavalier F. *Status of the DUNE project*. Rep., CNRS Nucl. Part. **https://atrium.in2p3.fr/nuxeo/nxfile/default/f6fdb622-c081-4320-a68e-b1088e87fdc3/blobholder:0/7-Docs-DUNE-Marchianni-Autiero-Duchesneau-Cavalier.pdf** (2021)
66. Lowe A, et al. *Instruments* 4:35 (2020)
67. Lowe A, et al. *Appl. Sci.* 11:9450 (2021)
68. Nomerotski A. *Nucl. Instrum. Methods A* 937:26 (2019)
69. Lowe AJ, et al. *Phys. Sci. Forum* 8:46 (2023)
70. Szelc AM. *J. Instrum.* 11:C02018 (2016)
71. Ali-Mohammadzadeh B, et al. *J. Instrum.* 15:T10007 (2020)
72. Agnes P, et al. *Phys. Lett. B* 743:456 (2015)
73. Auger M, et al. *J. Instrum.* 7:P05010 (2012)
74. Akerib DS, et al. *Nucl. Instrum. Methods A* 953:163047 (2020)
75. Andringa S, et al. *J. Phys. G* 50:033001 (2023)
76. Bezerra T, et al. *J. Phys. G* 50:060502 (2023)
77. Agnes P, et al. *J. Cosmol. Astropart. Phys.* 2103:043 (2021)
78. Abi B, et al. *Eur. Phys. J. C* 81:423 (2021)
79. Parsa S, et al. arXiv:2203.07501 [hep-ex] (2022)
80. Ajaj R, et al. *Phys. Rev. D* 100:022004 (2019)
81. Agnes P, et al. *Phys. Rev. D* 107:063001 (2023)
82. Moss Z, et al. arXiv:1604.03103 [physics.ins-det] (2016)
83. Howard B, et al. *Nucl. Instrum. Methods A* 907:9 (2018)
84. Howard B. *Toward a precision era of neutrino oscillation physics: liquid argon scintillation detector development for DUNE and neutrino oscillation studies with NOvA*. PhD Thesis, Indiana Univ., Bloomington (2019)
85. Macias C. *Neutrino hunting: looking through a UV lens*. PhD Thesis, Indiana Univ., Bloomington (2022)

86. Razeto A, et al. *J. Instrum.* 17:P05038 (2022)
87. Kuzniak M, Szelc AM. *Instruments* 5:4 (2020)
88. Aalseth CE, et al. *Adv. High Energy Phys.* 2015:541362 (2015)
89. Machado AA, et al. *J. Instrum.* 13:C04026 (2018)
90. Andreossi V, et al. *J. Instrum.* 19:C02021 (2024)
91. Souza HV, et al. *J. Instrum.* 16:P11002 (2021)
92. Brizzolari C, et al. *J. Instrum.* 16:P09027 (2021)
93. Auger M, et al. *Instruments* 2:3 (2018)
94. Anfimov N, et al. *J. Instrum.* 15:C07022 (2020)
95. Calivers L. *The 2x2 demonstrator: demonstration of a modular liquid argon detector for the DUNE Near Detector*. Presented at IPRD 2023, Siena, Italy, Sept. 25–29. **https://indico.cern.ch/event/1264216/contributions/5548299/** (2023)
96. Souza HV. *J. Instrum.* 18:C02029 (2023)
97. Huang H, Abbaszadeh S. *IEEE Sens. J.* 20:1694 (2020)
98. Liu K, Sakurai M, Aono M. *Sensors* 10:8604 (2010)
99. Ren T, et al. *Sci. Adv.* 8:4273 (2022)
100. Rooks M, et al. *J. Instrum.* 18:P01029 (2023)
101. Kunzmann J. (SoLAr Collab.) *J. Instrum.* 19:C02075 (2024)
102. Breskin A. *J. Phys. Conf. Ser.* 460:012020 (2013)
103. Erdal E, et al. *J. Instrum.* 14:P11021 (2019)
104. Tesi A, et al. *J. Instrum.* 16:P09003 (2021)